photonics

MDPI

Article

Monolithic Integration of an FP-SA Optical Spiking Neuron and SOA Synapse by Photonic Crystals

Haodong Xuan [1,2], Guangliang Sun [1,2], Yang Chen [1,2], Ningning Chen [1,2], Zeyu Wang [1,2], Hailing Wang [1,3,4,*] and Wanhua Zheng [1,2,3,4,*]

[1] Laboratory of Solid-State Optoelectronics Information Technology, Institute of Semiconductors, Chinese Academy of Sciences, Beijing 100083, China; hdxuan@semi.ac.cn (H.X.); sunguangliang@semi.ac.cn (G.S.); ychen@semi.ac.cn (Y.C.); cnn@semi.ac.cn (N.C.); zywang@semi.ac.cn (Z.W.)
[2] Center of Materials Science and Optoelectronics Engineering, University of Chinese Academy of Sciences, Beijing 100049, China
[3] Weifang Academy of Advanced Opto-Electronic Circuits, Weifang 261021, China
[4] College of Future Technology, University of Chinese Academy of Sciences, Beijing 101408, China
* Correspondence: hlwang07@semi.ac.cn (H.W.); whzheng@semi.ac.cn (W.Z.)

Abstract

We demonstrate a monolithically integrated photonic chip that combines an optical spiking neuron with a tunable synaptic element. The spiking neuron is realized using a quantum-well Fabry–Perot laser integrated with a saturable absorber (FP-SA), while a semiconductor optical amplifier (SOA) functions as a photonic synapse. Two photonic-crystal (PC) mirrors define the laser cavity and enable effective modulation of the synaptic weight. Experimental results further confirm the capability of the SOA for continuous and controllable synaptic weight tuning. This work represents an important step toward scalable on-chip photonic spiking neural networks.

Keywords: FP-SA; photonic crystal (PC); semiconductor laser; semiconductor optical amplifier; optical spiking neuron

1. Introduction

With the rapid advancement of artificial intelligence, conventional electronic processors based on the von Neumann architecture are increasingly challenged in meeting the growing computational demands [1]. Neuromorphic photonics has emerged as a promising alternative due to its advantages of high bandwidth, massive parallelism, and low energy consumption. A photonic neuromorphic system typically consists of optical neurons providing nonlinear activation and optical synapses implementing linear weighting.

Neuromorphic photonic computing requires the realization of both photonic synapses for linear operation and photonic neurons for nonlinear operation. In recent years, semiconductor laser-based optical spiking neurons have been extensively investigated, including vertical-cavity surface-emitting lasers with saturable absorbers (VCSEL-SAs) [2–4], distributed feedback lasers with saturable absorbers (DFB-SAs) [5–7], and graphene-based excitable lasers [8], as well as micro-ring lasers [9] and micro-disk lasers [10], all of which can provide strong nonlinear dynamics suitable for neuromorphic processing. In our previous work, we designed and fabricated a laterally coupled distributed feedback laser with a saturable absorber (LCDFB-SA) [11] operating as an optical neuron, and its underlying operating mechanism was investigated using time-domain traveling-wave simulations. In addition, linear computations have been successfully implemented in the optical domain

Check for updates

Received: 12 January 2026
Revised: 6 February 2026
Accepted: 19 February 2026
Published: 26 February 2026

Copyright: © 2026 by the authors. Licensee MDPI, Basel, Switzerland. This article is an open access article distributed under the terms and conditions of the Creative Commons Attribution (CC BY) license.

using Mach–Zehnder interferometers (MZIs) [12,13], micro-ring resonator (MRR) weight banks [14], phase-change materials (PCMs) [15] and SOAs [16,17]. Overall, FP-SA lasers offer a favorable balance between nonlinear dynamical richness, fabrication simplicity, and integration compatibility. Compared with VCSEL-based, DFB-based, microcavity-based, and emerging material platforms, FP-SA lasers are particularly well-suited for scalable and monolithically integrated neuromorphic photonic systems, owing to their simple cavity structure, strong excitable dynamics, and compatibility with on-chip integration of both photonic neurons and synapses.

Two-section semiconductor lasers constitute an important architecture for realizing photonic neurons. Among them, FP-SA lasers feature a simple structure and have been widely employed for photonic neuron implementations [5,18], demonstrating significant application potential. In addition, SOAs have also been successfully integrated and utilized as photonic synapses [19]. While SOA-based photonic synapses and FP-SA-based photonic neurons have both been demonstrated individually, their monolithic co-integration on a single chip with direct on-chip coupling has remained largely unexplored. Most existing demonstrations focus on either isolated neuron or synapse functionalities, or rely on hybrid integration schemes and external optical feedback paths, which limit scalability and system-level integration.

To address the challenges discussed above, we adopt two-dimensional photonic crystals (2D PCs) to achieve monolithic integration of an optical neuron and an optical synapse. Photonic-crystal structures offer high design flexibility, are not restricted by substrate material choice, and are fully compatible with standard planar semiconductor fabrication [20]. They are therefore considered a key enabling technology for the development of photonic integrated circuits (PICs). Compared with traditional distributed Bragg reflector (DBR) mirrors, 2D PCs provide increased freedom for integrating short-cavity lasers with more complex photonic-crystal-based optical devices such as wavelength-selective filters, ultra-compact bending waveguides, and multiplexing structures. As early as 2001, T. D. Happ et al. demonstrated the replacement of dielectric coatings with 2D PCs in in-plane InP-based micro-lasers with cavity lengths of 600–1000 μm, highlighting the feasibility of PC-based reflectors for integrated laser systems [21].

2. Device Structure and Fabrication

2.1. Device Structure

The schematic of the proposed device is shown in Figure 1a. The epitaxial wafer of the device is identical to that reported in Ref. [22]. The proposed integrated device consists of an SOA-FP-SA configuration with a total length of 1350 μm and a ridge width of 3 μm. The gain (GA) section is 1040 μm long, the saturable absorber (SA) section is 60 μm long, and the SOA synaptic section is 250 μm long. A ridge depth of 1.75 μm is selected to ensure single-transverse-mode operation. To minimize front-facet reflections, the SOA section is designed with a 7° curved waveguide [23]. A high-reflectivity PC mirror (PC1) is placed at the rear facet, while a low-reflectivity PC mirror (PC2) is located between the SOA and GA sections. In the PC regions, partial etching is required to satisfy fabrication constraints and maintain device performance. Unlike conventional FP-SA neuron lasers, the cavity facet on the right side of the SA in this device is coated with an anti-reflection (AR) coating, such that cavity formation relies on the photonic-crystal emission mirror rather than the cleaved facet.

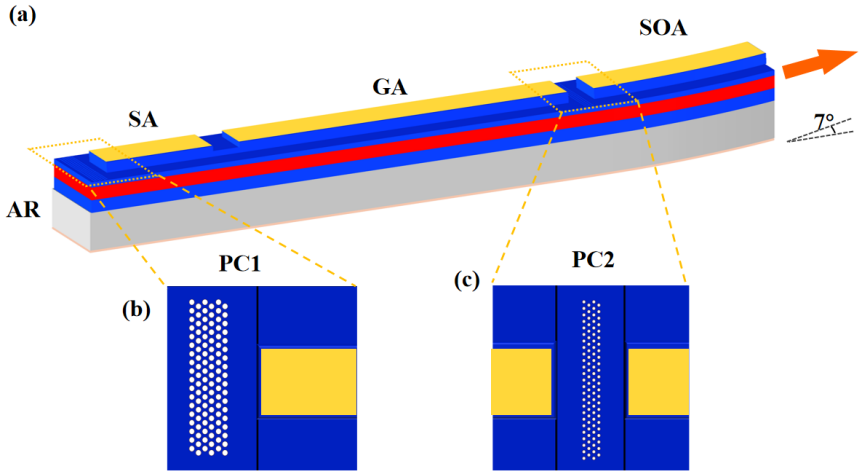


Figure 1. (**a**) Structure of the integrated SOA-FP-SA device. The arrows indicate the optical propagation directions. (**b**) PC1 formed at the rear facet for cavity feedback. (**c**) PC2 inserted between the SOA and GA sections.

For the PC2, partial transmission is straightforward to achieve by using small PC hole diameters. Thus, the primary design challenge lies in optimizing the PC1. To determine the appropriate PC hole radius and etch depth, we performed three-dimensional simulations using FDTD based on the actual epitaxial structure. Further simulations show that increasing the etch depth enhances reflectivity, reduces transmission, and lowers overall optical loss, as shown in Figure 2. However, deeper etching also introduces significant fabrication challenges: lower etch rates, degraded sidewall verticality, rapid shrinkage of hole diameter near the bottom due to InP etch characteristics, and increased process cost and variability. Moreover, if the etch depth is insufficient to reach the multiple quantum-well (MQW) layer, the refractive index modulation becomes too weak, leading to a substantial reduction in Bragg reflection strength. Thus, the selected etch depth represents a balance between optical performance and fabrication feasibility. The results indicate that a hole radius corresponding to an aperture of approximately 120 nm yields strong reflectivity at 1550 nm, with reduced reflectivity at wavelengths away from resonance. Therefore, the PC etch depth was set to 880 nm.

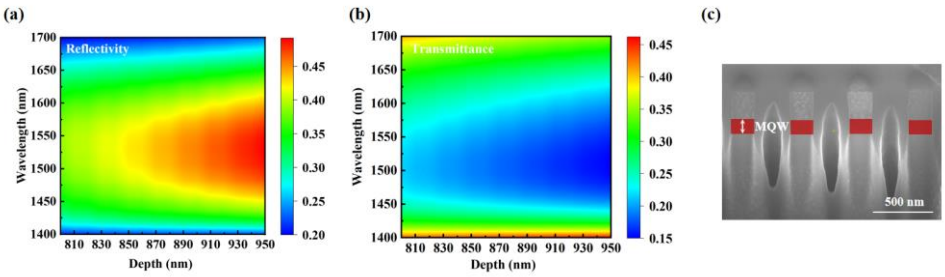


Figure 2. (**a**) Transmission spectra as a function of wavelength for PCs with different etching depths. (**b**) Reflection spectra as a function of wavelength for PCs with varying etching depth. (**c**) Cross-sectional scanning electron microscope (SEM) image of the etched two-dimensional photonic-crystal structure, showing the etched hole profile and its relative position with respect to the multiple quantum-well (MQW) active region.

2.2. Device Fabrication

Following the definition of the electrical isolation region between the GA and SA sections, the ridge waveguide is etched while simultaneously reserving a narrow trench for subsequent PC patterning. A 200 nm SiO_2 layer is deposited via plasma-enhanced chemical vapor deposition (PECVD), followed by spin-coating of ZEP520A electron-beam

resist. After electron-beam lithography (EBL) exposure and development, the PC pattern is transferred into the SiO_2 mask using reactive ion etching (RIE). Subsequently, the SiO_2 hard mask was etched using RIE, enabling pattern transfer into the hard mask layer. Inductively coupled plasma (ICP) etching is then employed to form the PC holes in the semiconductor. Devices fabricated with etching times of 90 s and 110 s exhibit inferior spectral performance compared with those etched for 100 s. Therefore, an etching duration of 100 s was adopted in the subsequent experiments to ensure optimal spectral characteristics. Next, an additional SiO_2 layer is deposited as insulation, and RIE is used again to define electrical injection windows. Ti/Au is sputtered to form the p-contact, with subsequent wet etching used to remove metal from the PC trenches to avoid excessive optical absorption. The substrate is thinned to 130 μm to reduce thermal resistance and improve heat dissipation. Au/GeNiAu metallization is deposited and annealed to form the n-contact.

3. Theoretical Model and Simulation Method

The spatiotemporal dynamics of the proposed device are investigated using a one-dimensional bidirectional traveling-wave model (TWM) [24,25]. The optical field propagating along the longitudinal direction z is expressed as the superposition of forward and backward-traveling waves under the slowly varying envelope approximation,

$$E(z,t) = f(z,t)e^{-i\,\omega_0 t} + b(z,t)e^{-i\,\omega_0 t}, \tag{1}$$

where $f(z,\ t)$ and $b(z,\ t)$ denote the complex envelopes of the forward- and backward-propagating fields, respectively.

The evolution of the optical fields is governed by the coupled traveling-wave equations

$$\frac{\partial f(z,t)}{\partial z} = \left[\frac{\Gamma g(z,t) - \alpha}{2} - i\Delta k(z,t)\right] f(z,t) + F_{sp(z,t)}, \tag{2}$$

$$\frac{\partial b(z,t)}{\partial z} = -\left[\frac{\Gamma\ g(z,t) - \alpha}{2} - i\ \Delta k(z,t)\right] b(z,t) + F_{sp(z,t)}, \tag{3}$$

where Γ is the optical confinement factor, α is the internal waveguide loss, $g(z,t)$ is the material gain, and $F_{sp}(z,t)$ represents the spontaneous emission noise that initiates the temporal dynamics. The carrier-induced wavevector detuning term $\Delta k(z,t)$ arises from refractive index modulation and is written as

$$\Delta k(z,t) = \left(\frac{2\pi}{\lambda}\right)\left[n_{eff(z,t)} - n_{eff,0}\right], \tag{4}$$

with $n_{eff,0}$ being the effective refractive index at transparency. The local photon density is defined as

$$s(z,t) = |f(z,t)|^2 + |b(z,t)|^2, \tag{5}$$

which directly couples the optical field to the carrier dynamics through stimulated emission and absorption processes. The temporal evolution of the carrier density in each active section is described by the carrier rate equation

$$\frac{\partial n(z,t)}{\partial t} = \frac{\eta I}{qV} - \frac{n(z,t)}{\tau(n)} - v_g g(z,t)s(z,t), \tag{6}$$

where I is the injection current, η is the injection efficiency, q is the elementary charge, V is the active volume, and v_g is the group velocity. The carrier lifetime $\tau(n)$ accounts for

nonradiative, radiative, and Auger recombination processes and is given by the standard *A*-*B*-*C* recombination model,

$$\tau(n) = \frac{1}{A + Bn + Cn^2}, \tag{7}$$

The material gain is modeled using a logarithmic dependence on the carrier density and includes gain saturation through a nonlinear compression term,

$$g(z,t) = \frac{g_0 \ln\left(\frac{n(z,t)}{n_t}\right)}{1 + \varepsilon s(z,t)}, \tag{8}$$

where g_0 is the gain coefficient, n_t is the transparency carrier density, and ε is the gain compression factor. Carrier-induced refractive index variations are incorporated through the linewidth enhancement factor, yielding

$$n_{eff}(z,t) = n_{eff,0} - \frac{\lambda}{4\pi} \Gamma \alpha_m \, g(z,t), \tag{9}$$

where α_m denotes the amplitude–phase coupling factor. Different functional sections of the device are represented by assigning distinct carrier parameters and injection conditions. The SOA and GA sections are electrically pumped and provide optical amplification, whereas the saturable absorber section is modeled without current injection and with a reduced effective carrier lifetime to represent fast carrier recovery under reverse bias. At low optical intensity, the SA introduces strong absorption, while at high photon density the absorption is saturated, leading to a reduction in intracavity loss. This dynamic modulation of the effective cavity loss gives rise to passive Q-switching behavior.

The coupling between the SOA and the main cavity is modeled using a photonic-crystal-based scattering interface. The photonic crystal is treated as a localized bidirectional coupler with predefined transmission and reflection coefficients. Assuming a power transmission of 60% and a reflection of 1%, the corresponding amplitude coefficients are expressed as

$$T_c = \sqrt{0.6}, \quad R_c = \sqrt{0.01}, \tag{10}$$

At the coupling interface, the optical fields satisfy the scattering relation

$$\begin{bmatrix} b_S \\ f_L \end{bmatrix} = \begin{bmatrix} R_c & T_c \\ T_c & R_c \end{bmatrix} \begin{bmatrix} f_S \\ b_L \end{bmatrix}, \tag{11}$$

where f_S is the forward-propagating field exiting the SOA, b_L is the backward-propagating field returning from the main cavity, b_S is the field coupled back into the SOA, and f_L is the field injected into the GA-SA cavity. The simulation parameters are summarized in Table 1. The device investigated in this work shares a high degree of structural similarity with the device reported in Ref. [11], including the material system and cavity configuration. Therefore, the corresponding parameters are primarily adopted from that reference.

Table 1. Simulation parameters.

Parameter	Value	Parameter	Value
A/s^{-1}	1×10^{8}	$\alpha_m/\mathrm{cm}^{-1}$	10
$B/\mathrm{cm}^3{\cdot}\mathrm{s}^{-1}$	1×10^{-10}	β	5×10^{-5}
$C/\mathrm{cm}^6{\cdot}\mathrm{s}^{-1}$	3.5×10^{-29}	$\varepsilon/\mathrm{cm}^3$	6×10^{-17}
λ/cm	1550×10^{-7}	Γ	0.08
$n_{eff,0}$	3.2	g_0/cm^{-1}	1500

Through the self-consistent solution of the coupled traveling-wave equations and carrier rate equations, the model captures the complete passive Q-switching cycle, including carrier accumulation, saturable absorber bleaching, pulse emission, and recovery dynamics. In this work, the synaptic weight is defined as the amplification effect of the SOA on the optical pulse amplitude injected into the photonic spiking neuron. By adjusting the SOA injection current, the gain experienced by the input optical pulses can be modulated, enabling multi-level modulation of the pulse amplitude. Importantly, the SOA is designed to primarily enhance the pulse amplitude while exerting a relatively weak influence on the pulse repetition frequency. Figure 3a shows the simulated dependence of the repetition frequency on the SOA injection current under different left-facet reflectivities. For all reflectivity conditions, the repetition frequency increases monotonically with increasing SOA current, indicating that the pulse emission rate can be effectively controlled by the SOA. Moreover, at a given SOA current, a higher left-facet reflectivity leads to a higher repetition frequency, with the difference becoming more pronounced at larger current values. Figure 3b presents the corresponding variation in the pulse amplitude as a function of the SOA injection current. In contrast to the repetition frequency, the pulse amplitude decreases with increasing left-facet reflectivity at the same SOA current, suggesting that stronger cavity feedback suppresses the energy buildup of individual pulses. These results reveal a trade-off between repetition frequency and pulse amplitude governed jointly by the left-facet reflectivity and the SOA injection current.

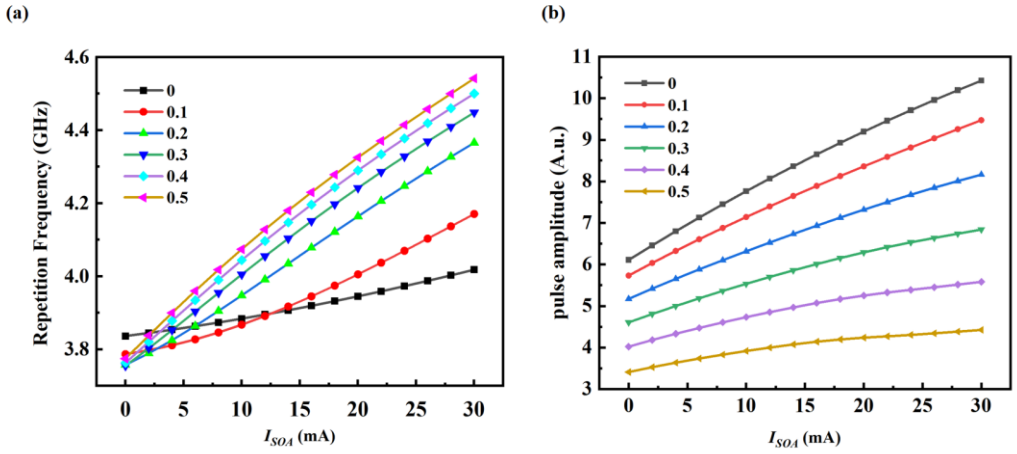


Figure 3. Simulated dependence of (**a**) the repetition frequency and (**b**) the pulse amplitude on the SOA injection current under different left-facet reflectivities, with the left-facet reflectivity varied from 0 to 0.5.

Furthermore, Figure 4 summarizes the relative variations in the pulse repetition frequency and pulse amplitude induced by increasing the SOA injection current from 0 to 30 mA under different left-facet reflectivities R_L. As R_L increases from 0 to 0.5, the relative change in repetition frequency at I_{SOA} = 30 mA with respect to 0 mA increases from 4.73% to 20.43%, whereas the relative change in pulse amplitude decreases from 70.61% to 29.74%. In other words, at relatively low left-facet reflectivities, the nonlinear influence on the pulse repetition frequency is weak, whereas the modulation of the pulse amplitude is more pronounced, which is favorable for synaptic weight modulation.

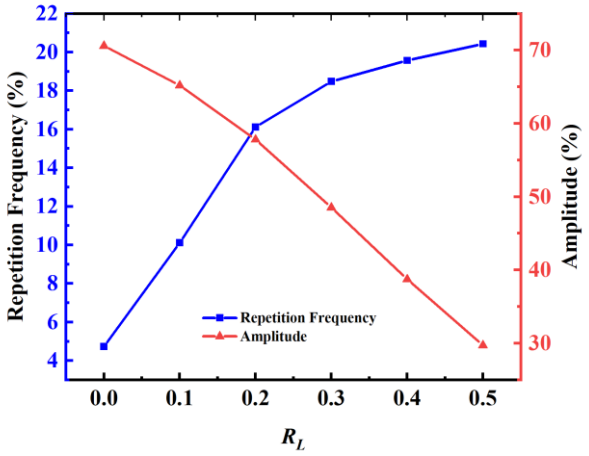


Figure 4. The relative variations in the pulse repetition frequency and pulse amplitude induced by increasing the SOA injection current from 0 to 30 mA.

It should be noted that photonic crystals exhibit pronounced wavelength-dependent behavior as well as spatially varying field distributions, which cannot be fully captured by constant coefficients. As a result, this simplification may affect the accuracy of the simulation results.

4. Results and Discussion

The experimental setup for characterizing the fabricated semiconductor optical spiking neuron and synaptic laser chip is illustrated in Figure 5. A forward bias is applied to the GA and SOA sections, while a reverse bias is applied to the SA section. In addition, a forward injection current is supplied to the SOA. The demonstrated device occupies a total area of approximately 0.675 mm^2, corresponding to a chip footprint of 1350 μm × 500 μm, indicating a relatively compact layout suitable for on-chip integration. After the electrical connections are completed, the output optical signal is coupled into a single-mode fiber (SMF). The fiber output is then connected to a 70 GHz high-speed photodetector (PD, XPDV3120R), and the resulting electrical signal is recorded using a real-time oscilloscope (Tektronix Inc., Beaverton, OR, USA, OSC, Tektronix DPO72304DX, 33 GHz).

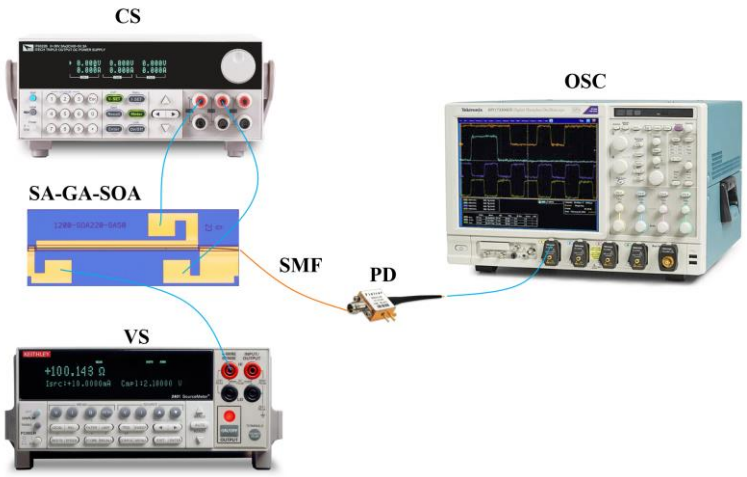


Figure 5. Experimental setup for characterizing the SA-GA-SOA integrated optical spiking neuron and synaptic laser chip. Forward current injection and reverse bias control are applied to the GA/SOA and SA, respectively. CS, multi-channel DC current source; VS, DC voltage source. The optical output is detected by a high-speed photodetector and analyzed using an oscilloscope.

First, the device was characterized by no current applied to the SOA and no bias voltage applied to the SA. The optical spectrum and output optical power were measured under these conditions. Figure 6a shows the measured Light–Current–Voltage (L−I−V) characteristics of the device. The threshold current is approximately 65 mA, and the output optical power reaches 23 mW at an injection current of 250 mA. For spectral characterization, the laser output was coupled into a single-mode optical fiber and measured using an optical spectrum analyzer. As shown in Figure 6b, the measured emission spectrum exhibits a dominant peak centered around 1570 nm with a side-mode suppression ratio (SMSR) of 26.42 dB. This phenomenon may originate from the combined effects of photonic-crystal mode selection and the composite cavity configuration.

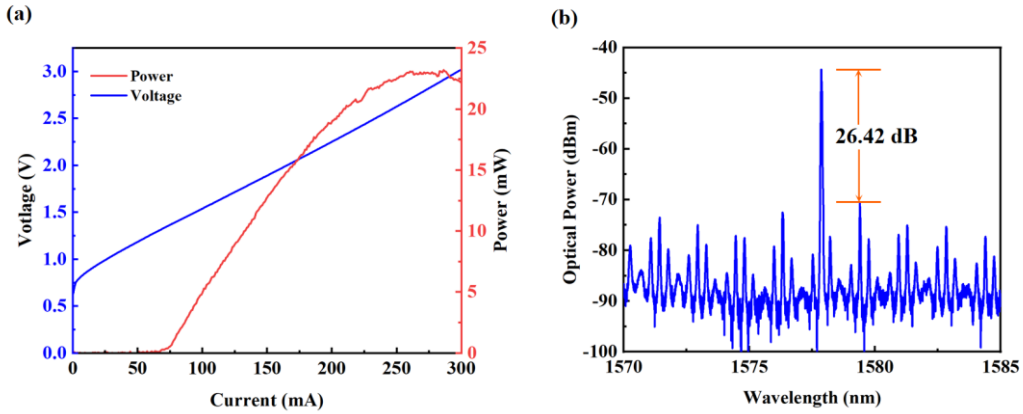


Figure 6. (**a**) L−I−V characteristics measured with no current injected into the SOA and no reverse bias applied to the SA. (**b**) Optical spectrum measured at a GA current of 150 mA.

Next, we characterize the output pulse behavior of the device and analyze the pulse repetition frequency and pulse amplitude. Figure 7 shows the evolution of the pulse repetition frequency as a function of the SOA injection current I_{SOA} for four GA bias currents (130 mA, 140 mA, 150 mA, and 160 mA), while the SA is maintained under a reverse bias of 1.6 V. It can be observed that increasing the current applied to the GA or the SOA leads to an increase in the pulse repetition frequency.

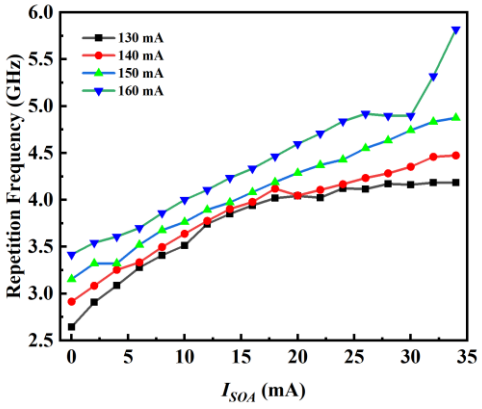


Figure 7. Repetition frequency versus SOA injection current I_{SOA} under different gain-section bias currents I_{GA}.

Figure 8a shows the dependence of the output pulse amplitude on the SOA injection current. As the SOA current increases, the pulse amplitude exhibits a clear and approximately linear growth trend. The blue square markers represent the experimental data, while the orange solid line corresponds to a linear fit, indicating that the SOA injection current

enables effective and multi-level modulation of the output pulse amplitude. Figure 8b presents representative time-domain pulse trains measured at different SOA injection currents (I_{SOA} = 0, 10, and 20 mA). As the SOA current increases, the pulse amplitude increases, while the pulse width remains nearly unchanged, with FWHM values of 9.99 ns, 9.72 ns, and 9.90 ns, respectively. The corresponding single-pulse energies at the device output are estimated to be 0.42 pJ, 0.46 pJ, and 0.55 pJ, respectively. With increasing I_{SOA}, the pulse amplitude is significantly enhanced, while the pulse sequence remains periodic and stable, indicating that the SOA injection current primarily modulates the pulse amplitude without noticeably affecting the temporal stability of the pulses. This behavior can be explained by the change in optical feedback conditions introduced by the SOA output facet reflectivity. When the reflectivity is reduced, less optical power is coupled back from the SOA into the GA–SA cavity, which weakens the feedback-induced perturbation to the laser oscillation frequency. Meanwhile, the reduced reflectivity increases the output coupling efficiency of the SOA, allowing more amplified optical power to be extracted. Consequently, the SOA predominantly contributes to pulse amplitude enhancement while exerting a diminished influence on the frequency characteristics.

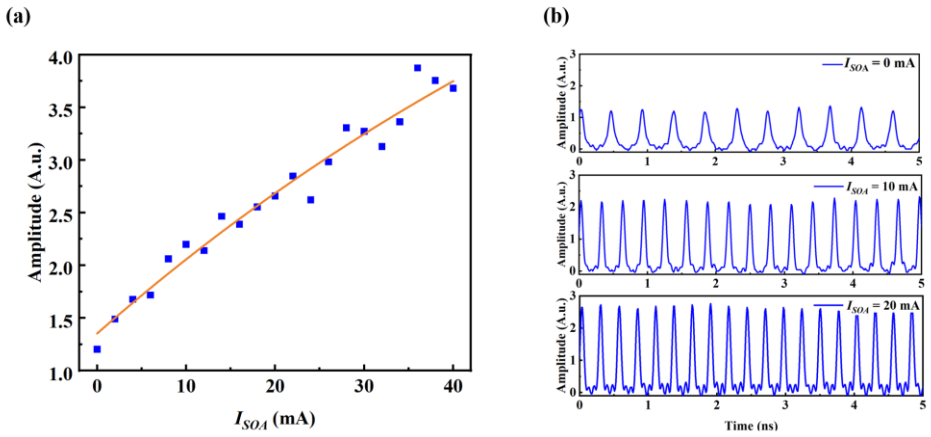


Figure 8. (**a**) Dependence of the output pulse amplitude on the SOA injection current I_{SOA} at I_{GA} = 120 mA and V_{SA} = 1.6 V. The blue square markers represent the experimental data, and the orange solid line shows a linear fit. (**b**) Representative time-domain pulse trains measured at different SOA injection currents at I_{GA} = 120 mA and V_{SA} = 1.6 V.

In the proposed GA–SA–SOA integrated device, thermal effects mainly originate from electrical injection in the gain and SOA sections. The resulting temperature variation can induce slow changes in the effective refractive index and cavity length, leading to a gradual shift in the emission wavelength. Nevertheless, the spiking dynamics investigated in this work occur on sub-nanosecond timescales, which are orders of magnitude faster than the thermal relaxation process. Therefore, thermal effects are not expected to significantly influence the fast spiking behavior, but may contribute to long-term drift under steady-state operation.

Due to the inevitable losses that occur during the coupling of the laser into a single-mode optical fiber, this coupling method results in a weak signal output from the laser chip. In addition, the electrode configuration is relatively complex. Further measurements of the pulse characteristics under the condition of anti-reflection coatings on both facets will be carried out in subsequent work. Moreover, deviations between the designed and experimentally realized PC reflectivities are unavoidable, resulting in discrepancies between simulation and experimental results. Overall, the device dynamics are jointly influenced by the reflectivity and transmissivity at both facets of the cavity, as well as multiple internal parameters, including the transmission and reflection characteristics of the PC, the

carrier lifetime in the SA region, and the injection current in the GA. Further experimental investigations will be carried out to optimize these characteristics and device performance.

5. Conclusions

In conclusion, a monolithically integrated photonic neuron-synapse system is demonstrated using two-dimensional photonic crystals, in which the SOA operates as an electrically tunable optical synapse and the FP-SA structure functions as an optical neuron. By introducing on-chip photonic-crystal structures with tailored reflectivity and transmissivity to replace conventional facet coatings, compatible integration of an optical spiking neuron and a tunable photonic synapse is achieved. Photonic crystals provide greater flexibility for subsequent device design due to their advantages in mode selection and fabrication compatibility. The output pulse characteristics under different injection currents were experimentally measured, and the observed phenomena were analyzed through numerical simulations, which further enabled the prediction of potential optimization pathways. This work provides a feasible approach toward scalable photonic spiking neural networks and advanced neuromorphic PICs.

Author Contributions: Writing—original draft preparation, H.X.; writing—review and editing, G.S., Y.C., N.C., Z.W., H.W. and W.Z. All authors have read and agreed to the published version of the manuscript.

Funding: This work was supported by National Key Research and Development Program of China (2022YFB2803104).

Institutional Review Board Statement: Not applicable.

Informed Consent Statement: Not applicable.

Data Availability Statement: Data are contained within the article.

Conflicts of Interest: The authors declare no conflicts of interest.

References

1. Shastri, B.J.; Tait, A.N.; Ferreira de Lima, T.; Nahmias, M.A.; Peng, H.-T.; Prucnal, P.R. Principles of Neuromorphic Photonics. In *Unconventional Computing*; Adamatzky, A., Ed.; Springer: Cham, Switzerland, 2018; pp. 83–118.
2. Alanis, J.A.; Robertson, J.; Hejda, M.; Hurtado, A. Weight adjustable photonic synapse by nonlinear gain in a vertical cavity semiconductor optical amplifier. *Appl. Phys. Lett.* **2021**, *119*, 201104. [CrossRef]
3. Nahmias, M.A.; Shastri, B.J.; Tait, A.N.; Prucnal, P.R. A Leaky Integrate-and-Fire Laser Neuron for Ultrafast Cognitive Computing. *IEEE J. Sel. Top. Quantum Electron.* **2013**, *19*, 1–12. [CrossRef]
4. Xiang, S.; Ren, Z.; Zhang, Y.; Song, Z.; Hao, Y. All-optical neuromorphic XOR operation with inhibitory dynamics of a single photonic spiking neuron based on a VCSEL-SA. *Opt. Lett.* **2020**, *45*, 1104–1107. [CrossRef]
5. Xiang, S.; Shi, Y.; Guo, X.; Zhang, Y.; Wang, H.; Zheng, D.; Song, Z.; Han, Y.; Gao, S.; Zhao, S.; et al. Hardware-algorithm collaborative computing with photonic spiking neuron chip based on an integrated Fabry–Perot laser with a saturable absorber. *Optica* **2023**, *10*, 162–171. [CrossRef]
6. Shi, Y.; Xiang, S.; Guo, X.; Zhang, Y.; Wang, H.; Zheng, D.; Zhang, Y.; Han, Y.; Zhao, Y.; Zhu, X.; et al. Photonic integrated spiking neuron chip based on a self-pulsating DFB laser with a saturable absorber. *Photonics Res.* **2023**, *11*, 1382–1389. [CrossRef]
7. Zheng, D.; Xiang, S.; Guo, X.; Zhang, Y.; Zeng, X.; Zhu, X.; Shi, Y.; Chen, X.; Hao, Y. Full-function Pavlov associative learning photonic neural networks based on SOA and DFB-SA. *APL Photonics* **2024**, *9*, 026102. [CrossRef]
8. Shastri, B.J.; Nahmias, M.A.; Tait, A.N.; Tian, Y.; Wu, B.; Prucnal, P.R. Graphene Excitable Laser for Photonic Spike Processing. *Opt. Lett.* **2015**, *40*, 4140–4143.
9. Vatsavai, S.S.; Sai Praneeth Karempudi, V.; Thakkar, I. An Optical XNOR-Bitcount Based Accelerator for Efficient Inference of Binary Neural Networks. In Proceedings of the 2023 24th International Symposium on Quality Electronic Design (ISQED), San Francisco, CA, USA, 5–7 April 2023; pp. 1–8.
10. Van Vaerenbergh, T.; Alexander, K.; Dambre, J.; Bienstman, P. Excitation transfer between optically injected microdisk lasers. *Opt. Express* **2013**, *21*, 28922–28932. [CrossRef]

11. Sun, G.; Chen, N.; Cao, P.; Wang, Z.; Xuan, H.; Chen, Y.; Wang, H.; Zheng, W. Single-mode photonic spiking neuron based on laterally coupled DFB laser with a saturable absorber. *Chin. Opt. Lett.* **2026**, *24*, 011407. [CrossRef]
12. Shen, Y.; Harris, N.C.; Skirlo, S.; Prabhu, M.; Baehr-Jones, T.; Hochberg, M.; Sun, X.; Zhao, S.; Larochelle, H.; Englund, D.; et al. Deep learning with coherent nanophotonic circuits. *Nat. Photonics* **2017**, *11*, 441–446. [CrossRef]
13. Zhou, H.; Zhao, Y.; Wang, X.; Gao, D.; Dong, J.; Zhang, X. Self-Configuring and Reconfigurable Silicon Photonic Signal Processor. *ACS Photonics* **2020**, *7*, 792–799. [CrossRef]
14. Tait, A.N.; de Lima, T.F.; Zhou, E.; Wu, A.X.; Nahmias, M.A.; Shastri, B.J.; Prucnal, P.R. Neuromorphic photonic networks using silicon photonic weight banks. *Sci. Rep.* **2017**, *7*, 7430. [CrossRef]
15. Feldmann, J.; Youngblood, N.; Karpov, M.; Gehring, H.; Li, X.; Stappers, M.; Le Gallo, M.; Fu, X.; Lukashchuk, A.; Raja, A.S.; et al. Parallel convolutional processing using an integrated photonic tensor core. *Nature* **2021**, *589*, 52–58. [CrossRef]
16. Shi, B.; Calabretta, N.; Stabile, R. Deep Neural Network Through an InP SOA-Based Photonic Integrated Cross-Connect. *IEEE J. Sel. Top. Quantum Electron.* **2020**, *26*, 1–11. [CrossRef]
17. Li, J.; Peng, L.; Li, S.-S.; Zhang, L.; Ding, X.; Jiang, L.; Zou, X.; Pan, W.; Yan, L. Photonic spiking neuron based on a single VCSEL with optical feedback. *Opt. Laser Technol.* **2025**, *181*, 111941. [CrossRef]
18. Zheng, D.; Xiang, S.; Li, N.; Zhang, Y.; Guo, X.; Zhu, X.; Chen, X.; Shi, Y.; Hao, Y. The Hybrid Photonic Convolutional Neural Networks Based on SOA and FP-SA. *J. Light. Technol.* **2024**, *42*, 8819–8825. [CrossRef]
19. Zhang, Y.; Xiang, S.; Cao, X.; Guo, X.; Han, G.; Hao, Y. Plastic Photonic Synapse Based on VCSOA for Self-Learning in Photonic Spiking Neural Network. *J. Light. Technol.* **2023**, *41*, 1759–1767. [CrossRef]
20. Noda, S.; Imada, M.; Okano, M.; Ogawa, S.; Mochizuki, M.; Chutinan, A. Semiconductor Three-Dimensional and Two-Dimensional Photonic Crystals and Devices. *IEEE J. Quantum Electron.* **2002**, *38*, 726–735. [CrossRef]
21. Happ, T.D.; Markard, A.; Kamp, M.; Gentner, J.L.; Forchel, A. InP-based short cavity lasers with 2D photonic crystal mirror. *Electron. Lett.* **2001**, *37*, 428–429. [CrossRef]
22. Wang, Z.; Sun, G.; Chen, N.; Wei, J.; Cao, P.; Xuan, H.; Wang, H.; Zheng, W. Quantum-well semiconductor laser based on a dumbbell-taper-enhanced optical field for optical frequency combs. *Chin. Opt. Lett.* **2025**, *23*, 121404. [CrossRef]
23. Guo, W.H.; Lu, Q.; Nawrocka, M.; Abdullaev, A.; O'Callaghan, J.; Donegan, J.F. Nine-channel wavelength tunable single mode laser array based on slots. *Opt. Express* **2013**, *21*, 10215–10221. [CrossRef] [PubMed]
24. Zhao, Y.; Shi, Y.; Li, J.; Liu, S.; Xiao, R.; Li, L.; Lu, J.; Chen, X. A Cascaded Tunable DFB Semiconductor Laser with Compact Structure. *IEEE J. Quantum Electron.* **2018**, *54*, 1–11. [CrossRef]
25. Wong, Y.L.; Carroll, J.E. A Travelling-Wave Rate Equation Analysis for Semiconductor Lasers. *Solid-State Electron.* **1987**, *30*, 13–19. [CrossRef]

Disclaimer/Publisher's Note: The statements, opinions and data contained in all publications are solely those of the individual author(s) and contributor(s) and not of MDPI and/or the editor(s). MDPI and/or the editor(s) disclaim responsibility for any injury to people or property resulting from any ideas, methods, instructions or products referred to in the content.